The Astrophysical Journal, 846:166 (16pp), 2017 September 10 https://doi.org/10.3847/1538-4357/aa8563

Evidence of a Bottom-heavy Initial Mass Function in Massive Early-type Galaxies from Near-infrared Metal Lines*

David J. Lagattuta[1], Jeremy R. Mould[2,3], Duncan A. Forbes[2], Andrew J. Monson[4,5], Nicola Pastorello[2,6], and S. Eric Persson[4]
[1] Univ Lyon, Univ Lyon1, Ens de Lyon, CNRS, Centre de Recherche Astrophysique de Lyon UMR5574, F-69230 Saint-Genis-Laval, France; david-james.lagattuta@univ-lyon1.fr
[2] Centre for Astrophysics & Supercomputing, Swinburne University, Hawthorn, VIC 3122, Australia
[3] ARC Centre of Excellence for All-sky Astrophysics (CAASTRO), Sydney, Australia
[4] Observatories of the Carnegie Institution of Washington, 813 Santa Barbara Street, Pasadena, CA 91101, USA
[5] Department of Astronomy & Astrophysics, The Pennsylvania State University, 525 Davey Lab, University Park, PA 16802, USA
[6] Deakin Software and Technology Innovation Laboratory, Deakin University, Burwood, VIC 3125, Australia
Received 2016 June 11; revised 2017 August 6; accepted 2017 August 7; published 2017 September 13

Abstract

We present new evidence for a variable stellar initial mass function (IMF) in massive early-type galaxies, using high-resolution, near-infrared spectroscopy from the Folded-port InfraRed Echellette spectrograph (FIRE) on the *Magellan* Baade Telescope at Las Campanas Observatory. In this pilot study, we observe several gravity-sensitive metal lines between 1.1 and 1.3 μm in eight highly luminous ($L \sim 10L_*$) nearby galaxies. Thanks to the broad wavelength coverage of FIRE, we are also able to observe the Ca II triplet feature, which helps with our analysis. After measuring the equivalent widths (EWs) of these lines, we notice mild to moderate trends between EW and central velocity dispersion (σ), with some species (K I, Na I, Mn I) showing a positive EW–σ correlation and others (Mg I, Ca II, Fe I) a negative one. To minimize the effects of metallicity, we measure the ratio $R = [\mathrm{EW(K\,I)/EW(Mg\,I)}]$, finding a significant systematic increase in this ratio with respect to σ. We then probe for variations in the IMF by comparing the measured line ratios to the values expected in several IMF models. Overall, we find that low-mass galaxies ($\sigma \sim 100$ km s^{-1}) favor a Chabrier IMF, while high-mass galaxies ($\sigma \sim 350$ km s^{-1}) are better described with a steeper (dwarf-rich) IMF slope. While we note that our galaxy sample is small and may suffer from selection effects, these initial results are still promising. A larger sample of galaxies will therefore provide an even clearer picture of IMF trends in this regime.

Key words: galaxies: elliptical and lenticular, cD – galaxies: evolution – galaxies: formation – galaxies: stellar content – stars: luminosity function, mass function

1. Introduction

The initial mass function (IMF) of stars is a key component in many areas of astrophysics, ranging from broad-scope topics such as galaxy formation and evolution (Davé et al. 2012), to more specific subjects like metallicity and star formation history (Maraston 2013). While many attempts to construct a "universal" IMF describing all galaxies have been made (see, e.g., Salpeter 1955; Kroupa 2001; Chabrier 2003), recent work suggests that the IMF may actually vary as a function of mass, (e.g., Treu et al. 2010; Conroy & van Dokkum 2012b; La Barbera et al. 2013; Ferreras et al. 2015; Spiniello et al. 2015) with high-mass galaxies becoming increasingly "bottom-heavy," i.e., described by an IMF with a larger-than-expected fraction of dwarf stars. Strengthening this argument is the fact that two largely independent methods: spectroscopic probes using gravity-sensitive line measurements and dynamical probes (such as gravitational lensing or stellar dynamics) measuring the stellar mass-to-light ratio Υ (e.g., Treu et al. 2010; Dutton et al. 2012; Cappellari et al. 2013; Posacki et al. 2015; Leier et al. 2016) have seen this trend. If true, this could have a significant effect on scaling relations such as the fundamental plane (Dutton et al. 2013; Mould 2014), altering our understanding of galaxy dynamics and dark matter mass fractions. Controversy on this subject remains very active, however (see, e.g., Smith 2014; Clauwens et al. 2015; Martín-Navarro et al. 2015b; Lyubenova et al. 2016).

It is worth noting, though, that spectroscopy-based studies often limit themselves to optical wavelengths, relying on a relatively small number of line features that lie below 1 μm. However, spectroscopic data taken at near-infrared (NIR) wavelengths have a number of advantages over their optical counterparts, especially where IMF-sensitive line features are concerned. In particular, several NIR absorption lines are gravity-sensitive (McLean et al. 2007; Deshpande et al. 2012; Smith et al. 2015) and have significantly different line strengths in giant and dwarf stars, making them well-suited to probe different stellar populations and expanding the pool of IMF tracers. Similarly, the flux of dwarf stars peak in the 1–2 μm range (Frogel et al. 1975), increasing the relative contribution of dwarf stars to the integrated galaxy light at these wavelengths. This in turn makes it easier to measure dwarf-sensitive absorption lines, allowing us to look for even fainter features. Furthermore, galaxy light is less sensitive to dust at NIR wavelengths, diminishing the effects of extinction, which can lower continuum-flux levels and decrease the signal-to-noise ratio (S/N) of detected lines.

In this paper, we present the initial results of the search for IMF-sensitive features at NIR wavelengths, using high-resolution spectroscopic data taken with the *Magellan* telescope. For our initial pilot data sample we select eight massive, highly luminous ($L_{\mathrm{gal}} \sim 10 \times L_*$), nearby galaxies, looking for trends in line strengths and line ratios as a function of galaxy mass. To fully explore the galaxy mass phase-space, we consider two possible mass tracers: total K-band luminosity (a proxy for stellar mass) and central velocity dispersion, a

* This paper includes data gathered with the 6.5 m *Magellan* Telescopes located at Las Campanas Observatory, Chile.

Table 1
Observing Log

Target Name	R.A.	Decl.	Obs. Date	Exp. Time (s)	Mean Airmass	Mean Seeing (″)
NGC 1316	03:22:41.789	−37:12:29.52	2014 Dec 12	5400	1.24	0.53
NGC 1332	03:26:17.321	−21:20:07.33	2014 Dec 13	5400	1.32	0.79
NGC 3258	10:28:53.588	−35:36:19.98	2014 Dec 13	3600	1.16	0.75
NGC 3557	11:09:57.653	−37:32:21.02	2014 Dec 12	3600	1.28	0.42
NGC 5845	15:06:00.787	+01:38:01.77	2014 Jun 15	3600	1.22	0.93
NGC 7014	21:07:52.185	−47:10:44.53	2014 Jun 15	7200	1.23	0.96
NGC 7410	22:55:00.945	−39:39:40.93	2014 Sep 14	5400	1.20	0.80
NGC 7743	23:44:21.130	+09:56:02.55	2014 Jun 15	7200	1.45	1.55

Table 2
Archival Galaxy Parameters

Galaxy	z[a]	σ_c[b] (km s^{-1})	$L_{\rm NIR}$[c] ($10^{12}\,L_\odot$)	$R_{\rm Tot}$[c] (″)	R_e[c] (″)	Slit Coverage[d] (%)
NGC 1316	0.00588	224.5	2.591	295.00	46.62	7.5
	(0.00005)	(3.3)	(0.029)		(2.29)	
NGC 1332	0.00510	312.5	0.504	182.50	27.02	13.0
	(0.00004)	(10.7)	(0.006)		(0.66)	
NGC 3258	0.00925	257.0	0.526	73.59	15.81	22.1
	(0.00005)	(12.7)	(0.007)		(0.58)	
NGC 3557	0.01023	260.1	2.546	126.37	26.13	13.4
	(0.00005)	(7.9)	(0.025)		(0.77)	
NGC 5845	0.00490	230.2	0.070	40.39	4.78	73.2
	(0.00006)	(8.1)	(0.001)		(0.09)	
NGC 7014	0.01618	292.8	0.741	56.46	11.21	31.2
	(0.00004)	(7.7)	(0.011)		(0.42)	
NGC 7410	0.00580	134.0	0.561	184.40	47.67	7.3
	(0.00009)	(12.4)	(0.006)		(0.43)	
NGC 7743	0.00562	84.7	0.176	93.23	29.97	11.7
	(0.00004)	(2.3)	(0.003)		(0.87)	

Notes.
[a] Average value from the NASA/IPAC Extragalactic Database (NED).
[b] Taken from the HYPERLEDA archive.
[c] Averaged from J-, H-, and K-band data in the 2MASS eXtended Source Catalog (XCS).
[d] Fraction of effective radius (R_e) covered by the FIRE slit.

direct probe of the galaxy's potential well. Comparing our equivalent width (EW) measurements to the predicted EW values of (IMF-dependent) theoretical models (e.g., Conroy & Gunn 2010a) we are able to account for the effects of IMF variation on EW, allowing us to probe IMF-sensitive trends as a function of mass. Furthermore, by studying EW ratios in addition to simple line strengths, we are also able to control for variables such as stellar age and metallicity.

This paper is organized as follows: in Section 2, we present the data and describe the steps we take to create reduced 1D spectra. In Section 3, we identify the lines used in this study and lay out the procedure for measuring EWs. We measure the actual EW values and search more mass-dependent trends in Section 4, and we compare the results to theoretical models in Section 5. We briefly summarize our results and conclude in Section 6. Throughout this work, we assume a standard cosmological model with $\Omega_\Lambda = 0.7$, $\Omega_M = 0.3$, and Hubble parameter $h = 0.7$.

2. Data and Reduction

2.1. Data Acquisition

We observed our galaxy sample using the Folded-port InfraRed Echellette spectrograph (FIRE; Simcoe et al. 2008) on the *Magellan* Baade telescope at Las Campanas Observatory. Data were acquired in good/fair conditions over several nights in 2014. The full list of observations can be seen in Table 1. Additionally, in Table 2, we present the physical parameters of each galaxy (taken from publicly available data archives), which were used to motivate the sample selection. These parameters are: redshift, central velocity dispersion (σ_c), total luminosity ($L_{\rm NIR}$), angular size ($R_{\rm Tot}$), and half-light radius (R_e). For all observations, we used FIRE in echellette mode with a 0.″6 slit width, providing wavelength coverage from 0.82 to 2.51 μm at a spectral resolution of $R = 6000$. The nominal slit length of FIRE is 7″. In order to maximize sensitivity while minimizing readout noise, we used the "High gain" (1.3 e$^-$ DN^{-1}) detector setting, limiting the exposure time of any single observation to 30 minutes to avoid detector saturation and nonlinear effects. "Science" frames (galaxies and telluric correction stars) were read out in Sample-Up-The-Ramp mode, while "Calibration" frames (arcs, flats, and twilight sky-flats) were read out in single-sample Fowler mode.

We observed telluric standards immediately following each target galaxy, in order to match atmospheric conditions of science objects as closely as possible. To choose the best

available telluric stars (which also served as a flux-calibrators), we used `find_tellurics`,[7] an internally provided script that scans a database of known A0V stars and looks for matches based on airmass and sky angle. For our galaxy sample, the typical best-matched stars had average V-band magnitudes $m_V \sim 9.5$, which were considerably brighter than the galaxies themselves. Thus, to again avoid saturation effects we only observed each telluric star for a total of 60 s (integrated over two 30 s exposures), along with a Thorium–Argon arc spectrum to provide a wavelength solution.

2.2. Reduction

Data reduction is primarily handled by FIREHOSE, an IDL-based pipeline designed specifically for FIRE data. While much of the pipeline is automated, there are a few times where we deviated from the standard output, which we briefly describe.

The pipeline first creates "master" quartz-lamp pixel-flats (for flat-fielding) and twilight flats (for illumination correction) from initial calibration data. During each observing night, we took five pixel-flat frames in the afternoon calibration session and two sky-flats during dawn twilight. The one exception to this was the first observing night (2014 June 5) where we took no sky-flat data, forcing us to substitute other sky frames for the reduction. After testing several options (either using sky frames taken during the other observing nights or publicly available archival data) we found no significant differences in any of the generated flat-field frames or science outputs. Therefore, in the final reduction for that night's data we used the flat-field files from the second observing night (2014 September 9), as it was the closest date to the original run.

After flat-fielding, the pipeline extracts the spectral trace from each frame, using an iterative process to fit the object profile, subtract sky flux, and attach a wavelength solution. We model the sky flux from the science frames themselves instead of separate sky frames, using the outermost 1″ regions at either end of the slit. This is to better account for the highly time-variable nature of the NIR sky. The extraction method is user-selected and can take the form of either an optimal, non-parametric window function or a simple boxcar function. We experimented with both methods for our data, comparing the results of each case. The optimal extraction method produced spectra that were less noisy and contained fewer cosmic-ray artifacts, but (even after flux calibration) had very disjointed inter-order continuum-flux levels. Conversely, the boxcar method had much smoother continuum levels, but were noisier. To obtain the best reduction possible, then, we combine elements of each extraction method in the final product. In particular, we use the optimally extracted traces, but re-scale them to the boxcar-extracted continuum levels before analyzing them.

Following extraction, the data are flux-calibrated and corrected for telluric absorption using the procedure implemented in the xtellcor package (Vacca et al. 2003). Finally, the extracted, calibrated 2D data are collapsed to 1D, and all data frames for a given science target are combined using a weighted average. Individual echelle orders are then stitched together (using an inverse-variance weighting scheme) into a final spectrum. An example of the final output can be seen in Figure 1.

[7] http://web.mit.edu/~rsimcoe/www/FIRE/ob_manual.htm#Tellurics

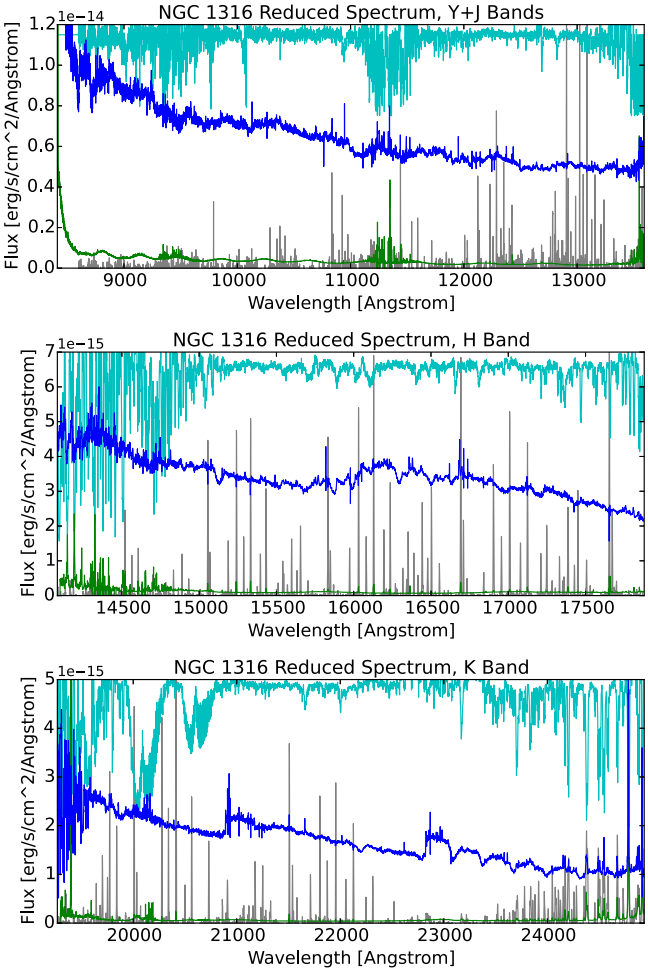

Figure 1. Reduced 1D spectrum of the nuclear region of NGC 1316, the massive AGN-host galaxy in the Fornax cluster, and one of the eight galaxies used in this study. The observed spectrum is shown in blue, while the error spectrum (multiplied by a factor of 10) is shown in green. The error spectrum is upscaled simply to make it more visible in the plot. We also show a scaled sky emission spectrum (gray) and telluric absorption spectrum (cyan) to better highlight areas of increased sky noise. In the "cleanest" wavelength regions with few sky lines and high atmospheric transmission, the typical S/N/Angstrom is ∼100. In other regions where sky noise is high or instrument sensitivity is low (at bluer wavelengths) the S/N can fall to as low as 10–20.

3. Line Measurements

3.1. Line Selection

3.1.1. M-dwarf Metal Lines

To probe for variations in the IMF, we look for M-dwarf absorption features in our galaxy spectra. McLean et al. (2007) and Deshpande et al. (2012) identify a number of these features between 1.1 and 1.3 μm, giving us a wide range of lines to choose from. In order to avoid the complicated physics of molecular rotation, however, we limit ourselves to neutral atomic lines. Following Deshpande et al. (2012), we only select lines with an oscillator strength $\log(gf) > -2$ and continuum line-depth $D > 0.2$, as this maximizes the chance that the feature will be detected in the integrated galaxy spectrum. After applying these criteria, we are left with 18 candidate absorption lines. The full list of features, along with rest-frame wavelengths (measured in air), is shown in Table 3.

To check for IMF variability in these features, we generate a series of synthetic stellar population (SSP) models with

Table 3
Target M-dwarf Atomic Line Features

Element	Rest-frame Wavelength[a] (Å)	Plot Color[b]
K I	11690.2	black
K I	11769.6	black
K I	11772.8	black
Fe I	11783.3	magenta
Mg I	11828.1	cyan
Fe I	11882.8	magenta
Ti I	11892.9	orange
Fe I	11973.0	magenta
K I	12432.3	black
K I	12522.1	black
Na I	12679.1	red
Ti I	12738.4	orange
Pa-β	12821.7	green
Ti I	12847.0	orange
Mn I	12899.8	brown
Al I	13123.4	gray
Ca I	13134.9	yellow
Al I	13150.8	gray

Notes.
[a] Measured in air.
[b] Color used to identify this element group in subsequent plots.

different IMF slopes and compare line strengths between models. To remove metallicity effects to the first order, we sum all lines of a given element together and then divide by the combined Fe I line strength. This makes the results largely insensitive to metallicity in the $-0.3 < [\mathrm{Fe/H}] < 0$ range of models. We do note that additional testing shows that the strength of these lines is much more dependent on IMF and stellar age than metallicity (see Section 5), suggesting that this normalization procedure will not significantly change the results. However, we choose to include it in this work anyway, to remove as many external factors from the analysis as possible. From this exercise, we find that K I shows the most IMF sensitivity, though other lines (such as Mg I, Na I, and Al I) also show moderate trends. As expected, these are low ionization potential elements. Because of this, much of the analysis and discussion in this work focus on these select features (especially K I), though we include the results of all the candidate lines for completeness.

3.1.2. The Calcium-II Triplet

Thanks to the large wavelength range of FIRE, we can also detect the Ca II triplet feature at λ[8498,8542,8662] Å, which provides a number of added benefits to the analysis. First, Ca II is known to be sensitive to the IMF (Saglia et al. 2002; Cenarro et al. 2003), giving us an independent check to the M-dwarf analysis. Second, the line-depth of Ca II is significantly stronger than the dwarf lines, making identification much easier. Finally, the S/N of the feature (again considerably higher than the dwarf lines) is high enough to estimate a velocity dispersion, which can be used as a proxy for mass.

All lines (identified in every galaxy) can be seen in Figure 2.

3.1.3. Rejected IMF-sensitive Tracers

In addition to the M-dwarf metal lines and Ca II triplet, previous studies have identified other IMF-sensitive spectral lines at NIR wavelengths that could, in principle, be used as additional constraints. However, due to redshift, S/N, and/or modeling effects, were were unable to include them in our data set.

1. The Na I doublet λ[8183,8195] (e.g., Schiavon et al. 1997a; van Dokkum & Conroy 2012) falls slightly outside of the FIRE wavelength coverage for our galaxy sample, except for the highest-redshift galaxies ($z > 0.0007$). Because we were not able to measure the line for all of our targets, we did not include it in this work.
2. The Wing-Ford λ9916 FeH band (e.g., Schiavon et al. 1997b; McConnell et al. 2016) is covered by the FIRE spectra, but its broad, shallow shape makes it difficult to distinguish from local continuum variations. Additionally, since FeH is a molecular feature, we reject it in favor of simpler atomic absorption lines. This is because, although the diatomic molecule FeH is included in the synthetic spectra of Allard et al. (2012) that we use to compare to the observation, there is a danger that its detailed line list is incomplete. This requires further investigation. For now we would recommend using empirical spectral libraries (such as MILES) where FeH is used as an IMF indicator, rather than synthetic. But it is also important to study the metallicity dependence of FeH bands, as it is likely to follow the behavior of CaH, which is stronger in metal-poor subdwarfs than solar metallicity main-sequence stars.
3. Finally, the Na I λ11400 (Smith 2014) line falls in a telluric water absorption band (11100–11500 Å) for all of our galaxy sample redshifts, making it impossible to accurately measure its line strength.

3.2. Measuring Lines

3.2.1. The Ca-II Procedure

After identifying lines of interest, we then model and measure their equivalent widths (EWs). Since the Ca II lines are always the strongest absorption features seen, we independently model these features before moving on the fainter M-dwarf lines.

First, we model galaxy kinematics using the penalized pixel-fitting routine (pPXF) described in Cappellari & Emsellem (2004). For reference spectra, we use the Tremonti et al. (2004) galactic templates (constructed from the Bruzual & Charlot 2003 stellar population libraries), rescaled to match the resolution of our FIRE data. This provides an estimate of redshift and central velocity dispersion. At the median redshift of our galaxy sample, the FIRE slit aperture ($7'' \times 0.''6$) corresponds to a physical size of $\sim(1 \times 0.1)$ kpc.

To make an initial guess for the fit parameters, we use the "best" redshift estimate taken from the NASA/IPAC Extragalactic Database (NED) and small-aperture velocity dispersion measurements from the HYPERLEDA[8] archive (Makarov et al. 2014). In most cases, the best-fit pPXF redshift is within 50 km s^{-1} of the NED value, but there are a few instances (NGC 3258 and NGC 5845) where the shift is more substantial ($\sim$150 km s^{-1}). To test for asymmetry in the line profile, we also run the pPXF fit with a more general model, modifying the

[8] http://leda.univ-lyon1.fr/

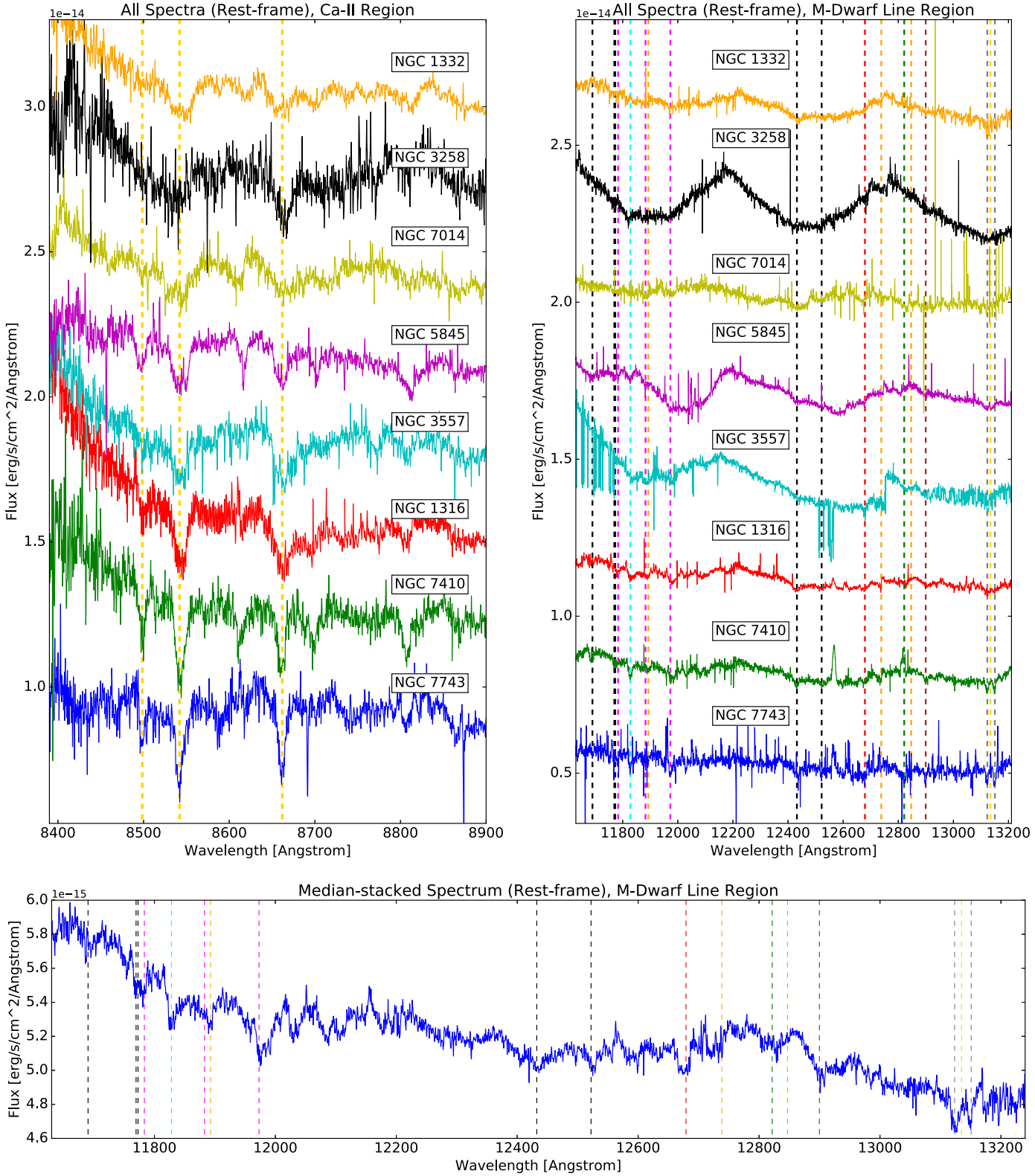

Figure 2. Cutout spectral regions from each galaxy in our sample, identifying the lines used to probe for IMF variations. Top left: the portion of the spectra containing the strong Ca II-triplet. Yellow dashed lines identify each absorption feature. Top right: the spectral region containing the faint M-dwarf lines. Dashed lines again represent the location of absorption features and follow the order of elements presented in Table 3. The element identified by each dashed line is given by its color, according to the following: black = K I, magenta = Fe I, cyan = Mg I, orange = Ti I, red = Na I, green = Paβ, brown = Mn I, gray = Al I, yellow = Ca I. Spectra are ordered from bottom to top based on increasing central velocity dispersion, and a distinct trend between dispersion and line-depth (especially with Ca II) is clearly visible. To make line identification easier, we shift each spectrum to the rest-frame. Additionally, each spectrum has been arbitrarily offset along the flux axis to prevent features from overlapping. Bottom: the median-stacked average of all spectra, covering the M-dwarf line region. Here, the absorption features used in this work are clearly visible.

initial Gaussian-fit-shape with higher-order Gauss–Hermite polynomial terms, following, e.g., van der Marel & Franx (1993) and Cappellari & Emsellem (2004). By including the first two terms (h_3 and h_4) we do alter the best-fit velocity dispersion, but this change is small (typically between 5 and 10 km s^{-1}) and is always within the measurement uncertainty of the Gaussian fit. The redshift of the fit remains virtually unchanged. As this result is minor, we adopt the Gaussian model parameters for the rest of the fitting procedure, especially since the M-dwarf lines do not have a high enough S/N to accurately measure profile asymmetry.

After measuring the redshift, we convert the observed spectra to rest-frame and extract a small (500 Å) cutout, centered between the Ca II λ8542 and Ca II λ8662 lines. This provides enough data to model both the Ca II absorption and the surrounding continuum flux. We fit the continuum with a third-order polynomial spline model, then divide the cutout by this model to normalize the flux. After normalizing, we "invert" the spectrum (Inverse = 1 − Normalized) to remove the continuum, leaving only the inverted absorption features.

The model of the Ca II system is relatively simple, consisting of a set of three Gaussians, one for each absorption feature. While the amplitudes of each line vary independently, we fix the σ value to match the pPXF fit. Prior to measuring final EWs, however, we convolve the data and models to a common velocity dispersion $\sigma = 350$ km s^{-1}, in order to account for kinematic broadening effects. Additionally, we allow the redshift of the system to vary, ensuring that the Gaussian peak finds the center of the absorption features and eliminating any systematic errors in the wavelength solution. In general, the difference between the Gaussian-fit redshift and the pPXF value is small (again $<$10 km s^{-1}), but accounting for this extra shift makes later identification of dwarf lines much easier, since many of these features are just at or above the level of the noise leading to possible misidentification or confusion.

The model is optimized though a standard chi-square minimization process, using a Levenberg–Marquardt algorithm to explore parameter space. Once the Ca II parameters are optimized, we create the new best-fit Ca II model and simply sum the flux of each individual Gaussian to obtain the EW of the line. To estimate model uncertainty, we add Poisson noise to the spectrum and re-run the fit. After repeating this process 500 times, we combine the results, taking the standard deviation of the set to be the model error. An example of the full fitting procedure can be seen in Figure 3, and the Ca II EW values are shown in Table 4.

To check the accuracy of our measurement technique, we also calculate EW values for each Ca II feature using the line-strength indices presented in Table 1 of Conroy & van Dokkum (2012a). We find excellent agreement between the two methods, and in all cases the difference between the EW of the line index and our fitting technique is within the statistical uncertainty of the model. In some ways this is expected because our model-fitting technique is designed to mimic the classical approach, but with a slightly modified continuum fit. Regardless, the agreement suggests our procedure is robust and that we can confidently use it to fit the other metal lines, which do not have formally defined line indices.

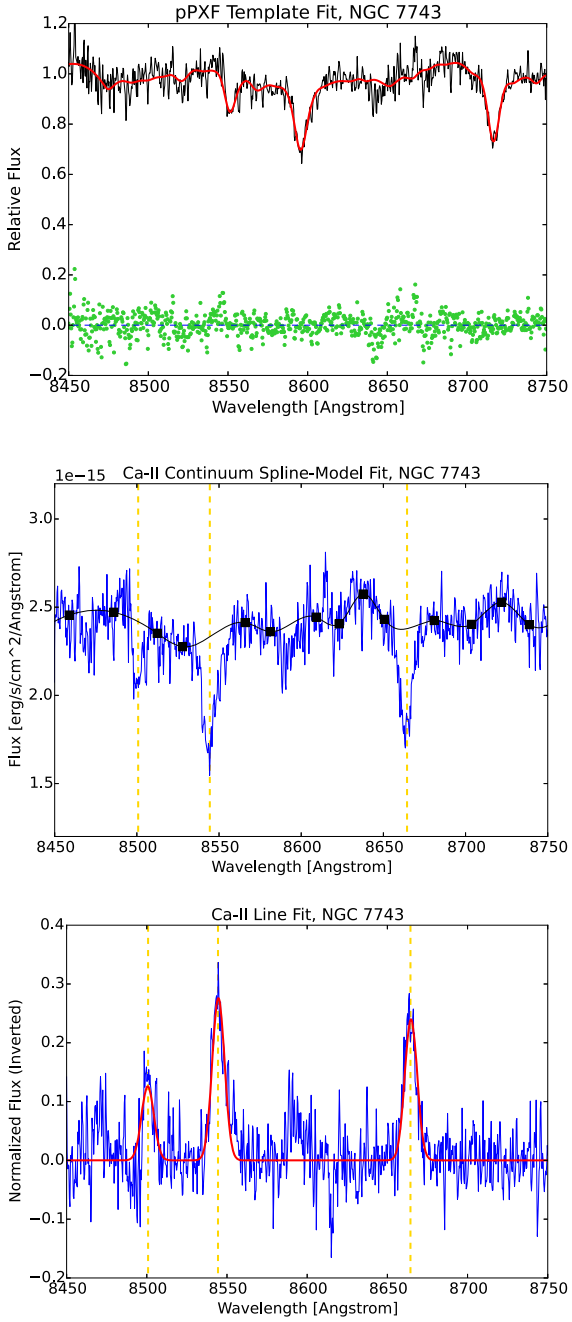

Figure 3. Example of the Ca II fitting procedure, applied to NGC 7743. Top: kinematic and redshift data are fit with the pPXF modeling code (Cappellari & Emsellem 2004), using Bruzual & Charlot (2003) galaxy templates. The real spectrum is shown in black, while the model template is shown in red. Residuals are represented as green dots. Middle: we model the continuum flux surrounding Ca II, using a third-order polynomial spline function. The absorption features (represented by dashed yellow lines) are clearly visible. Before fitting, the spectrum is shifted to the rest-frame using the the best redshift value from the pPXF fit. Bottom: the spectrum is normalized by the continuum model, then inverted (taking 1 − Normalized flux), leaving only the Ca II feature. We fit this feature with a series of Gaussians (using the pPXF σ value as the FWHM), which we use to measure an equivalent width (EW). Simultaneously, we measure a new best-fit redshift value that we use to better identify central positions of M-dwarf absorption lines. EW values obtained from the model fits are shown in Table 4.

3.2.2. Other Lines

The fitting and measuring procedure for the dwarf lines largely follows that of Ca II, though there are some modifications based on the Ca II fit. Starting again with the observed-frame spectrum, we shift the data to the new rest-frame, as determined by the best-fit model redshift. This new

Table 4
Best-fit Model Parameters and Equivalent Width Values

Galaxy	z	σ (km s^{-1})	M_K	Ca II λ8498	Ca II λ8542	Ca II λ8662	K I λ11690	K I λ11770	K I λ11773	Fe I λ11783	Mg I λ11828	Fe I λ11883	Ti I λ11893	Fe I λ11973	K I λ12432	K I λ12522	Na I λ12679	Ti I λ12738	Pa-β λ12822	Ti I λ12847	Mn I λ12900	Al I λ13123	Ca I λ13135	Al I λ13151
NGC 1316	0.00601	206.0	−25.39	1.19	3.27	2.48	0.37	0.00	0.46	0.35	1.02	0.69	0.32	1.62	1.09	0.37	0.94	0.11	1.21	0.20	0.95	1.26	0.00	0.98
	(0.00001)	(12.7)	(0.02)	(0.03)	(0.12)	(0.10)	(0.02)	(0.00)	(0.04)	(0.03)	(0.03)	(0.04)	(0.02)	(0.08)	(0.05)	(0.01)	(0.04)	(0.01)	(0.05)	(0.02)	(0.05)	(0.07)	(0.05)	(0.04)
NGC 1332	0.00540	353.0	−24.00	0.73	2.73	1.71	0.00	1.02	0.18	0.00	0.74	0.35	0.00	1.46	1.33	0.11	1.26	0.00	0.95	0.33	0.99	2.22	0.00	0.98
	(0.00002)	(45.2)	(0.02)	(0.03)	(0.21)	(0.12)	(0.00)	(0.23)	(0.14)	(0.04)	(0.06)	(0.05)	(0.00)	(0.11)	(0.11)	(0.02)	(0.12)	(0.01)	(0.18)	(0.12)	(0.09)	(0.20)	(0.14)	(0.10)
NGC 3258	0.00960	319.0	−23.79	0.88	1.99	3.47	0.09	0.07	0.10	0.00	0.73	0.17	0.00	0.58	1.33	0.81	1.07	1.15	0.82	0.10	1.17	1.84	0.00	0.64
	(0.00003)	(40.8)	(0.02)	(0.08)	(0.16)	(0.22)	(0.05)	(0.17)	(0.15)	(0.00)	(0.09)	(0.05)	(0.00)	(0.05)	(0.16)	(0.07)	(0.09)	(0.11)	(0.10)	(0.06)	(0.12)	(0.16)	(0.07)	(0.09)
NGC 3557	0.01027	233.0	−25.27	0.30	1.77	3.33	0.24	0.00	0.49	0.00	0.72	0.13	0.00	1.21	0.85	0.16	0.76	0.78	1.09	0.58	0.67	2.11	0.23	1.09
	(0.00002)	(16.2)	(0.02)	(0.01)	(0.06)	(0.15)	(0.03)	(0.02)	(0.06)	(0.01)	(0.05)	(0.04)	(0.00)	(0.08)	(0.05)	(0.02)	(0.02)	(0.03)	(0.04)	(0.01)	(0.04)	(0.15)	(0.08)	(0.04)
NGC 5845	0.00555	239.0	−21.75	1.70	2.58	1.49	0.86	0.66	0.03	0.23	0.97	0.53	0.00	1.10	0.91	0.00	0.61	0.02	1.25	0.00	0.97	1.10	0.27	0.21
	(0.00001)	(9.4)	(0.02)	(0.02)	(0.06)	(0.02)	(0.02)	(0.02)	(0.05)	(0.04)	(0.02)	(0.07)	(0.00)	(0.02)	(0.06)	(0.00)	(0.01)	(0.01)	(0.04)	(0.00)	(0.05)	(0.04)	(0.00)	(0.02)
NGC 7014	0.01637	305.0	−24.34	0.51	2.66	1.18	0.54	0.00	0.36	0.20	0.55	0.84	0.16	1.26	1.41	0.26	2.11	1.34	1.61	0.00	2.10	1.07	0.62	0.00
	(0.00003)	(35.0)	(0.03)	(0.06)	(0.27)	(0.12)	(0.13)	(0.11)	(0.17)	(0.16)	(0.13)	(0.14)	(0.16)	(0.15)	(0.16)	(0.17)	(0.21)	(0.16)	(0.19)	(0.17)	(0.12)	(0.24)	(0.26)	(0.19)
NGC 7410	0.00597	124.0	−24.04	1.40	3.03	1.96	0.38	0.42	0.09	0.26	1.04	0.10	0.29	0.85	0.75	0.53	0.60	0.27	0.00	0.14	0.76	1.07	0.17	1.06
	(0.00001)	(5.7)	(0.02)	(0.03)	(0.10)	(0.05)	(0.02)	(0.01)	(0.01)	(0.01)	(0.03)	(0.02)	(0.01)	(0.03)	(0.03)	(0.02)	(0.03)	(0.02)	(0.00)	(0.01)	(0.03)	(0.04)	(0.03)	(0.03)
NGC 7743	0.00566	85.7	−22.74	0.98	1.99	1.76	0.03	0.36	0.00	0.48	0.80	0.44	0.37	0.96	0.57	0.27	1.08	0.22	0.98	0.08	0.74	0.95	0.09	1.11
	(0.00001)	(8.2)	(0.03)	(0.05)	(0.14)	(0.12)	(0.01)	(0.01)	(0.01)	(0.02)	(0.04)	(0.02)	(0.01)	(0.06)	(0.07)	(0.02)	(0.09)	(0.02)	(0.11)	(0.02)	(0.04)	(0.05)	(0.03)	(0.05)

redshift accounts for the small shift between the Gaussian and pPXF fit values, as mentioned in the previous section. We then extract the full spectral range containing the dwarf lines, from $\lambda = 11500$ Å to $\lambda = 13500$ Å and fit a spline model to measure the continuum. Rather than fit the continuum around each line individually, we construct a full spline model over the entire wavelength range, as many of the lines fall close to one another, leaving insufficient continuum for a proper fit. To ensure a consistently "clean" set of continuum points for each galaxy, we make use of the Meneses-Goytia et al. (2015) galaxy templates, looking for points close to the lines that do not fall on any other absorption or emission features. To better match the models to our galaxy sample, we convolve the initial template with a Gaussian kernel equal to the galaxy's velocity dispersion (typically around 300 km s^{-1}), making sure that the selected continuum points do not overlap the real signal. In most cases, the model-selected continuum points are unchanged from galaxy to galaxy; however, in the case of known active galactic nuclei (AGNs; NGC 1316, NGC 7410, and NGC 7743), [Fe II] emission coincides directly with the continuum point at $\lambda = 12566$ Å, leading to a poor fit and affecting the EW measurements of nearby K I λ12522 and Na I λ12679. To avoid this problem, we simply remove that point from the fit and replace it with two new points immediately longward and shortward of the emission line. This eliminates the fitting error in the region without significantly changing the fit in any other location.

After creating this new continuum model, we again normalize and invert the spectrum, allowing us to fit and measure the dwarf-line EWs. This process is also quite similar to the Ca II model, though we eliminate the redshift parameter and fix the σ value to match the best-fit Ca II value. We optimize the new model (consisting of a set of 18 Gaussian amplitudes) using the same χ^2-minimization algorithm and then re-run the process with Poisson errors to obtain uncertainties. Finally, we recreate all of the best-fit models and sum up the model fluxes to obtain EW values for each line. This process is repeated for every galaxy in the sample, an example of which is shown in Figure 4. The complete fitting results are shown in Table 4.

4. Analysis

Trends between EW measurements and galaxy parameters (such as age, mass, and environment) are caused by a variety of factors. While many are due to variations in chemical abundance, stellar age, and metallicity, other effects can be caused by changes in the IMF. To find evidence of a variable IMF, we first look for trends between the EW data and physical properties of the host galaxies, then compare the results to theoretical models in order to account for the other, more obvious factors (Section 5).

Total mass, in particular, is an interesting quantity since previous studies have demonstrated correlations between IMF slope and galaxy mass (e.g., Dutton et al. 2012; Spiniello et al. 2012; Ferreras et al. 2015; Martín-Navarro et al. 2015a; Spiniello et al. 2015). Though there are potentially many ways to measure mass, we focus here on two complementary methods. In the first case, we measure the K-band luminosity of each galaxy, assuming it to be a robust tracer of stellar mass (e.g., Kauffmann & Charlot 1998). In the second case, we take the best-fit velocity dispersion (determined from the pPXF fit) as the mass proxy, as it directly probes the galaxy's central potential well.

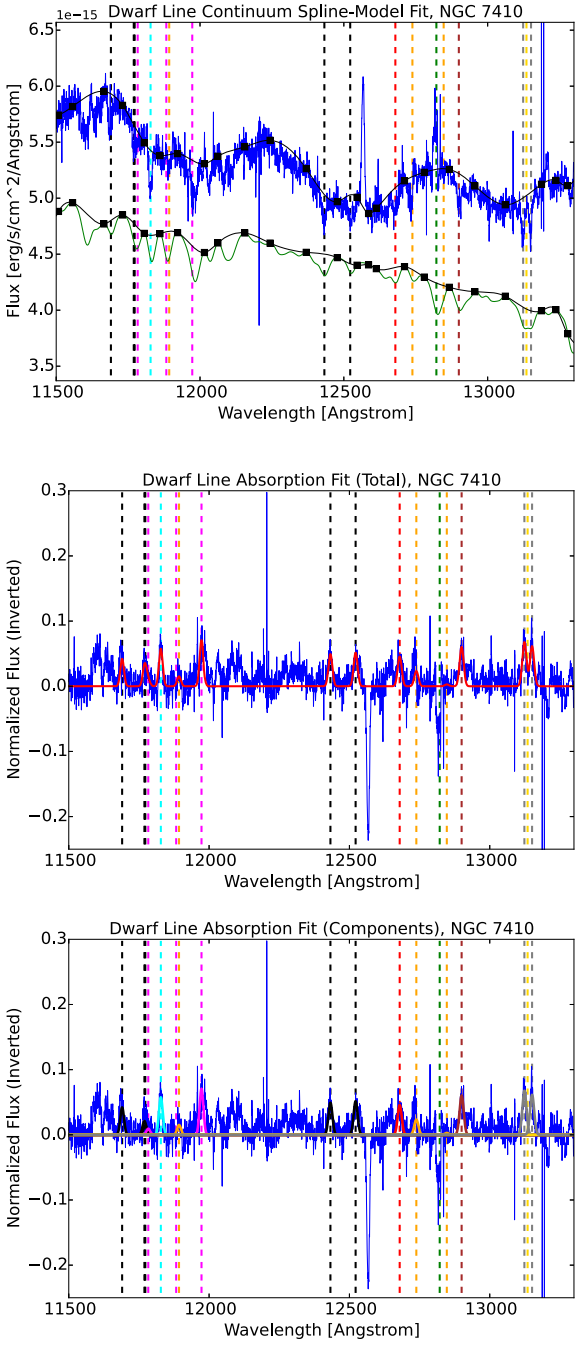

Figure 4. Example of the M-dwarf line fitting procedure, using NGC 7410. The method is very similar to the Ca II fit shown in Figure 3. Top: a spline function models the continuum, using the Meneses-Goytia et al. (2015) SSP galaxy templates to locate "clean" continuum points close to the lines of interest. Real data are shown in blue, while the SSP template (re-scaled to match the flux level of the real data) is shown in green. The knot-points of the spline model are represented by black squares, and the actual spline fits to the data and template appear as a black lines. Middle: the continuum is removed and each line is modeled with a Gaussian to measure an equivalent width. The redshift and σ-value of each Gaussian are fixed (based on the results of the Ca II fit), but the amplitudes are free to vary. The best-fit model, measuring all lines simultaneously, is shown in red. Bottom: same as the middle panel, but individual line components are shown. The colors of each line component are the same as those used in Figure 2.

We then fit trend lines between mass and EW for each element (both Ca II and the dwarf lines), using a standard least-squares minimization technique that accounts for measurement errors in both directions. In instances where an element has

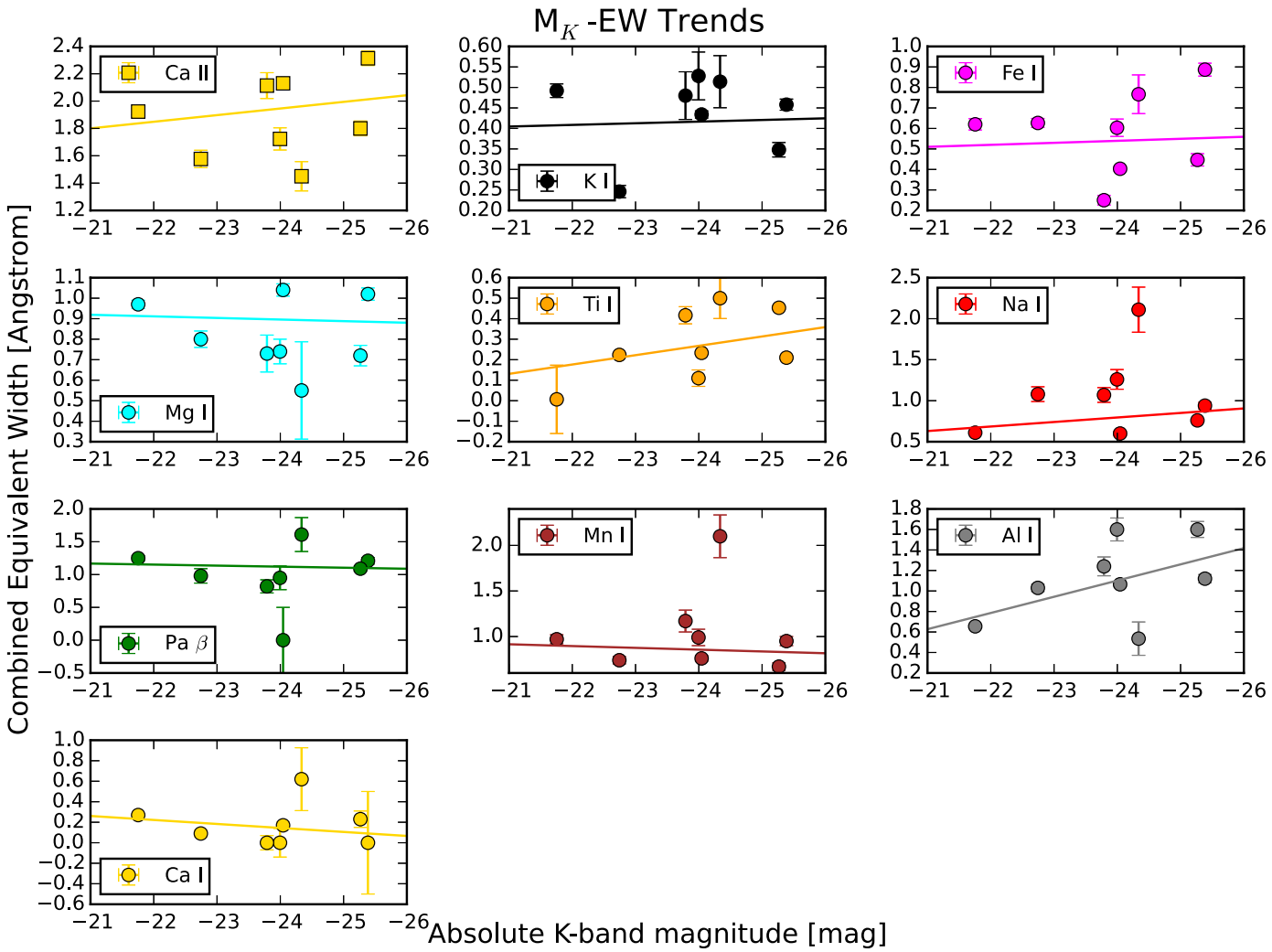

Figure 5. Measured equivalent width (EW) values for the metal lines used in our sample, as a function of K-band luminosity. Elements that have multiple line features (e.g., Ca II and K I) are summed together to reduce noise. A best-fit trend line for each element is also shown, given by the equation $\mathrm{EW} = m_{\mathrm{Mag}} \times M_{\mathrm{K}} + b_{\mathrm{Mag}}$. Fit parameters for each line can be found in Table 5. While some elements do show a slight correlation between luminosity and EW, these trends tend to be weak and highly sensitive to scatter.

more than one observed absorption feature (i.e., Ca II, K I, Fe I, Ti I, and Al I), we sum all lines together to create a "master" EW, in order to reduce noise. Figure 5 shows the results of the luminosity–EW fit over the eight galaxies in our sample. While trends do exist for certain elements (e.g., Na I and Al I), the slopes are often weak and possibly driven by one or two extreme outliers. This fact, coupled with noisy data and a small sample size, makes it difficult to make a definitive statement on the relationship between luminosity and EW.

On the other hand, the trends between EW and velocity dispersion (σ; Figure 6) are stronger, with some elements (K I, Na I, and Mn I) having a clear positive (EW–σ) correlation and others (Ca II, Mg I, and Pa-β) a negative one. The fit parameters for the trends seen in Figures 5 and 6 are presented in Table 5. Following van Dokkum & Conroy (2012), a positive σ–EW correlation suggests that a line is dwarf-sensitive, while a negative correlation suggests it is giant-sensitive. Thus, a negative slope for Ca II (a known giant-sensitive line) is expected, as are positive slopes for K I, Na I, and Mn I. The negative slopes for the other lines could imply that they are giant-sensitive as well. However, we stress that a positive (or negative) EW–σ trend alone cannot fully address IMF variability, and comparisons to theoretical models accounting for age and metallicity are better suited to answer this question. Regardless, given that the EW–σ correlation is nominally stronger than that of EW–Luminosity (in agreement with previous work by Graves et al. 2009), we choose to use σ as our mass tracer (and hence IMF tracer) for the remainder of this work. To do this, though, we will need to compare our results to known IMF-sensitive models (e.g., Conroy & Gunn 2010a).

5. Models

To probe IMF-dependency using models, we have written a high-resolution post-processor for the Flexible Stellar Population Synthesis (FSPS) code base (Conroy et al. 2009; Conroy & Gunn 2010b). We begin by running FSPS normally, specifying metallicity (Z) and IMF parameters in the usual way without changing the built-in libraries of evolutionary tracks. There are only ~30 wavelength points in the range between 11500 and 13500 Å in FSPS, however, and we need hundreds to probe at the FIRE resolution. Therefore, our post-processor substitutes the M star atmosphere fluxes of Allard et al. (2012) for the built-in flux libraries of FSPS at effective temperatures below 7000 K. This approach has the advantage that the synthesis uses precise values of temperature, surface gravity, and

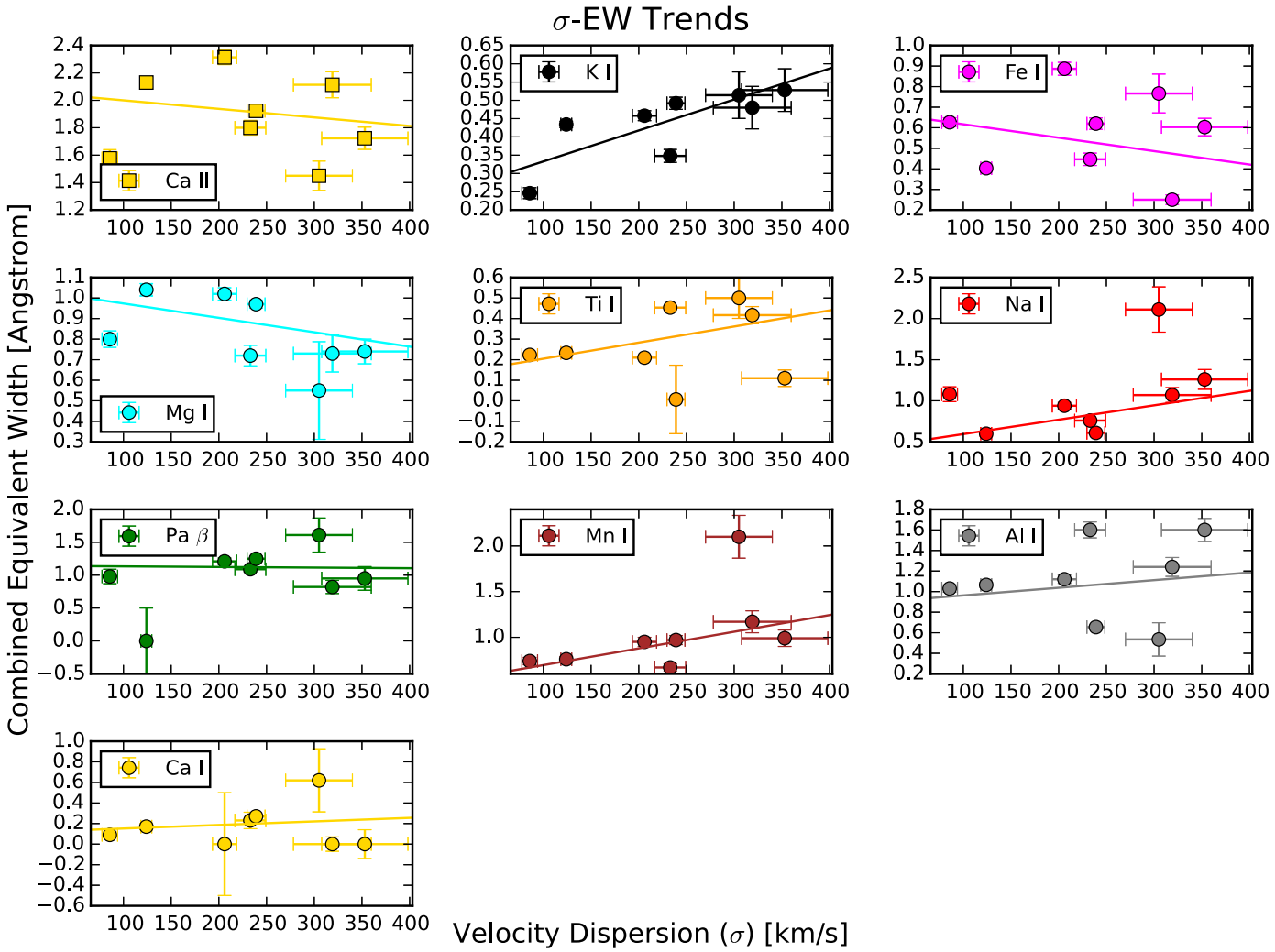

Figure 6. Same as Figure 5, but with velocity dispersion (σ). Here, the trends are considerably more significant. As expected, giant-sensitive features like Ca II show a negative correlation between σ and EW, while dwarf-sensitive features have a positive correlation. Here, the equation of the trend line is given by $\mathrm{EW} = m_\sigma \times \sigma + b_\sigma$, and fit parameters are again presented in Table 5.

metallicity sampled as finely as necessary. At higher temperatures we simply interpolate the low-resolution fluxes.

As previously mentioned, the principal parameters controlling a galaxy's stellar spectrum are expected to be metallicity, star formation history, IMF, and detailed chemical composition. A useful parameterization of elemental composition is the α/Fe ratio, as supernova yields lead to such a scaling. A full investigation of early-type galaxy stellar spectra would employ techniques such as principal component analysis to prioritize a moderate set of parameters, such as metallicity, age, IMF slope, and α/Fe ratio. Such an investigation is beyond the scope of the present work with its small sample, and we instead focus only on first-order variations in IMF slope. However, our library of synthetic spectra will permit α/Fe ratio and age to be investigated when a large S/N ≈ 100 sample becomes available. The present work is a pathfinder for the telescope resources, both optical and infrared, required for that study.

Spectra for stellar models at dwarf-star temperatures ($\sim$3100 K) are shown in the top panel of Figure 7. Along with a model with solar metallicity (black line), an additional variant with $Z = Z_\odot/3$ ([M/H] $= -0.5$ dex) is shown in red. A low-temperature (2500 K) model, also at solar metallicity, is presented for reference (blue line). Looking at the ratio between the black and red lines (green line), we see that for M dwarf temperatures the metallicity dependence of the main-sequence flux is weak. This is due to the line opacity and continuum opacity scaling in a similar way with metallicity. The K I line, however, becomes very strong at L dwarf temperatures. Folding this information into an integrated galaxy spectrum, we show the final SSP models for both the $Z = Z_\odot$ and $Z = Z_\odot/3$ cases, assuming a Salpeter IMF, in the middle panel of Figure 7. Here, we see a slightly more significant dependence on metallicity when main-sequence flux is included. However, the effect is still relatively small and does not account for all of the EW variation seen in the data, leaving room for potential IMF effects. We probe for these effects directly in the bottom panel of Figure 7, where we replace the low-metallicity Salpeter model with a solar-metallicity Chabrier model (cyan line). While the overall ratio is still close to unity, there is a noticeably larger variance between the depths of the metal lines in this case, suggesting that IMF may play a larger role in determining their EWs. However, while the IMF variation is larger than the metallicity variation, both effects are still weak: in all but the most extreme cases, the typical change in line strength from model to model is less than 5%.

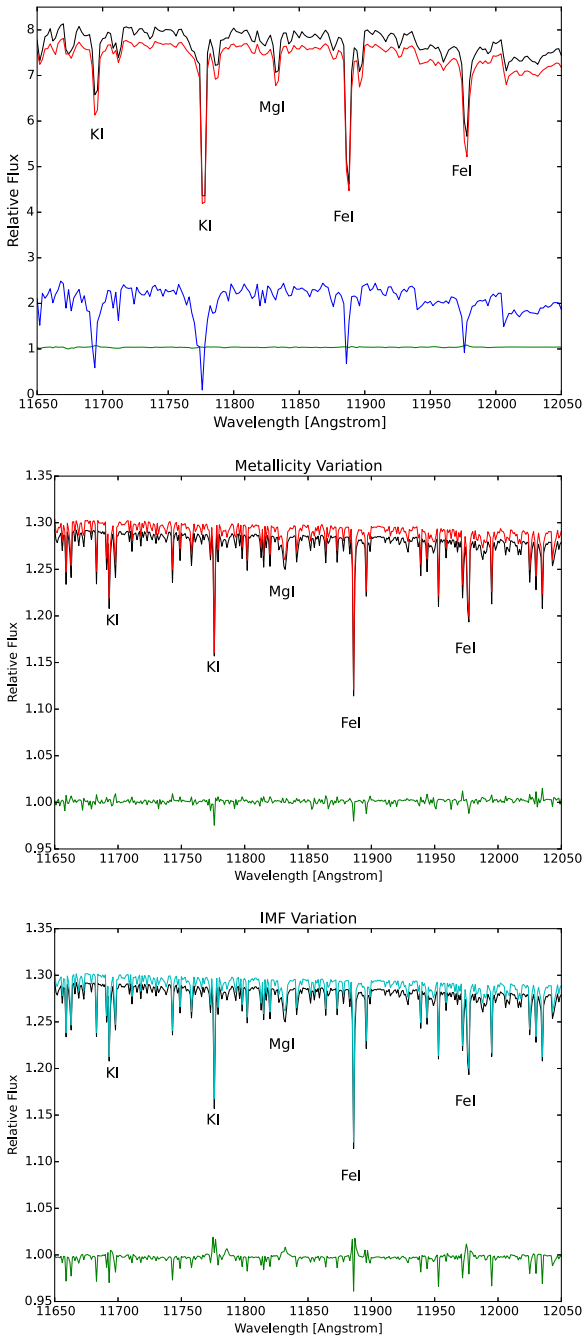

Figure 7. Top: combined Allard et al. (2012) model atmosphere spectra for 3000 K + 3100 K, log(g) = 5. Broadening of 50 km s^{-1} has been added. The black spectrum is the model for solar metallicity and the red one for [M/H] = −0.5 dex. These are ratioed in the green spectrum. The blue spectrum is for effective temperature 2500 K. Middle: SSP models generated from the Allard et al. (2012) spectra, assuming a Salpeter IMF and a stellar age of 10 Gyr. Line colors are the same as in the top panel. We see that a changing metallicity has an effect on EW values, though this effect is small. Bottom: similar SSP model comparison, but the low-metallicity model has been replaced by a solar-metallicity model with a Chabrier IMF (cyan line). Comparing the ratio lines of the middle and bottom panels, we see a larger variance in the IMF test compared to the metallicity test, suggesting that a varying IMF may play a larger role in the observed EW trends. We note, however, that both effects are still small (<5% for nearly all lines of interest). In all panels, the positions of some metal lines used in this work are highlighted for reference.

Using a series of these synthetic spectra, each generated with a different model IMF, we measure theoretical EW values for both the Ca II triplet and the M-dwarf metal lines, which we compare to the observed data. To be as consistent as possible, we measure model EWs using the technique outlined in Section 3.2, and like the observed data, we smooth the models to a common velocity dispersion $\sigma = 350$ km s^{-1}. EWs for all lines are recorded in Table 6. For our choice of IMF, we use all five IMF codes of Conroy & Gunn (2010b), namely, Salpeter (1955), Kroupa (2001), Chabrier (2003), van Dokkum (2008), and Davé (2008), along with an additional dwarf-rich variant. The dwarf-rich model takes the form of a broken power law, with a steep slope ($\alpha = 4.3$) at the low-mass end ($0.08M_{\odot} < M_{\rm star} < 0.5M_{\odot}$), and a shallower slope ($\alpha = 2.3$) at higher masses ($M_{\rm star} > 0.5M_{\odot}$.) (For comparison, Salpeter 1955 has a single power-law slope $\alpha = 2.35$.) While this low-mass slope parameterization is considerably steeper than the $\alpha \sim 3$ slope observed in other early-type galaxies (e.g., Spiniello et al. 2014; Conroy et al. 2017), this is an intentional choice: by including a model with a super-abundance of dwarf stars, we have a larger baseline for comparing models, allowing us to more easily understand and isolate the IMF's role in line-strength variation. A graphical representation of each IMF model can be seen in Figure 8.

Table 5
EW Trend Fit Results

Line	$m_{\rm Mag}$	$b_{\rm Mag}$	$\chi^2_{\rm Mag}$	m_σ	b_σ	χ^2_σ
Ca II	−0.0485	0.78	6.75	−0.0006	2.06	7.06
	(0.0713)	(1.69)		(0.0013)	(0.29)	
K I	−0.0040	0.32	1.97	0.0008	0.25	0.95
	(0.0291)	(0.70)		(0.0003)	(0.07)	
Fe I	−0.0098	0.30	7.51	−0.0007	0.68	7.00
	(0.0674)	(1.61)		(0.0008)	(0.18)	
Mg I	0.0078	1.08	2.63	−0.0007	1.04	2.20
	(0.0404)	(0.96)		(0.0006)	(0.14)	
Ti I	−0.0456	−0.83	2.94	0.0008	0.13	2.90
	(0.0451)	(1.09)		(0.0006)	(0.12)	
Na I	−0.0551	−0.53	7.32	0.0018	0.42	6.89
	(0.0609)	(1.45)		(0.0014)	(0.31)	
Pa β	0.0158	1.50	2.45	−0.0001	1.14	2.50
	(0.0478)	(1.15)		(0.0012)	(0.29)	
Mn I	0.0197	1.33	5.43	0.0018	0.51	3.62
	(0.0708)	(1.69)		(0.0010)	(0.20)	
Al I	−0.1580	−2.69	5.66	0.0007	0.89	11.14
	(0.0645)	(1.52)		(0.0015)	(0.31)	
Ca I	0.0389	1.08	1.25	0.0003	0.12	1.46
	(0.0325)	(0.74)		(0.0005)	(0.11)	

In Table 6, we measure EWs for both solar and subsolar metallicity parameters, though we limit stellar age to single-burst populations between 10 and 13 Gyr in order to keep the total parameter space small. These ages are expected to match well with the stellar ages of our galaxy sample. The metallicity dependence of the EWs is visible in the table, as are somewhat larger dependencies on stellar age and IMF.

We highlight the effects of metallicity and stellar age on various line strengths in Figure 9. From the plot, we see slight trends between line EW and metallicity, though the effect is minimal and EW remains largely flat between subsolar and solar models. As a sanity check, we do see a mild increase in Fe I EW with increasing metallicity, which is to be expected given the iron-based metallicity variations we employ. A stronger effect can be seen with stellar age, where the older models show consistently smaller EWs. To account for IMF effects we include three different IMF codes: Chabrier (green

Table 6
Model-predicted Equivalent Widths Å

IMF[a]	Ca II	Ca II	Ca II	K I	K I	K I	Fe I	Mg I	Fe I	Ti I	Fe I	K I	K I	Na I	Ti I	Pa β	Ti I	Mn I	Al I	Ca I	Al I	$\sum$(Ca II)	$\sum$(K I)	$\sum$(Fe I)	$\sum$(Ti I)	$\sum$(Al I)
$Z = Z_{\odot}$, Age = 10 Gyr																										
0	0.56	1.27	1.20	0.52	0.04	0.77	0.12	0.69	1.17	0.36	0.92	0.25	0.17	0.19	0.21	0.48	0.12	0.16	0.94	0.10	0.48	3.03	1.75	2.22	0.69	1.43
1	0.56	1.29	1.22	0.45	0.03	0.64	0.09	0.66	1.14	0.34	0.91	0.21	0.13	0.18	0.20	0.51	0.10	0.15	0.92	0.09	0.42	3.07	1.46	2.15	0.64	1.35
2	0.61	1.39	1.30	0.49	0.03	0.67	0.09	0.70	1.20	0.34	0.97	0.21	0.16	0.18	0.20	0.52	0.10	0.15	1.02	0.09	0.46	3.31	1.56	2.27	0.64	1.48
3	0.56	1.29	1.22	0.45	0.03	0.61	0.09	0.61	1.06	0.31	0.84	0.21	0.13	0.15	0.17	0.47	0.09	0.12	0.83	0.09	0.40	3.07	1.43	1.99	0.57	1.23
4	0.61	1.39	1.30	0.49	0.03	0.67	0.09	0.70	1.20	0.34	0.97	0.21	0.16	0.18	0.20	0.52	0.10	0.15	1.02	0.09	0.46	3.31	1.56	2.27	0.64	1.48
5	0.60	1.18	1.17	0.52	0.17	0.80	0.27	0.74	1.19	0.40	0.89	0.33	0.32	0.31	0.21	0.40	0.15	0.26	1.14	0.17	0.78	2.94	2.15	2.35	0.75	1.92
$Z = Z_{\odot}/3$, Age = 10 Gyr																										
0	0.56	1.27	1.21	0.51	0.07	0.79	0.12	0.68	1.14	0.37	0.91	0.24	0.17	0.16	0.22	0.48	0.10	0.15	1.04	0.09	0.50	3.04	1.79	2.16	0.68	1.54
1	0.56	1.30	1.23	0.44	0.05	0.64	0.09	0.64	1.10	0.33	0.89	0.20	0.13	0.16	0.20	0.49	0.09	0.14	0.98	0.09	0.43	3.09	1.45	2.08	0.62	1.40
2	0.60	1.37	1.31	0.44	0.05	0.67	0.10	0.66	1.16	0.37	0.95	0.20	0.13	0.16	0.23	0.52	0.10	0.17	1.10	0.13	0.47	3.27	1.49	2.21	0.70	1.57
3	0.58	1.28	1.23	0.40	0.05	0.57	0.08	0.57	1.00	0.30	0.82	0.17	0.11	0.13	0.17	0.46	0.09	0.12	0.92	0.09	0.41	3.09	1.29	1.91	0.56	1.32
4	0.60	1.37	1.31	0.44	0.05	0.67	0.10	0.66	1.16	0.37	0.95	0.20	0.13	0.16	0.23	0.52	0.10	0.17	1.10	0.13	0.47	3.27	1.49	2.21	0.70	1.57
5	0.60	1.19	1.18	0.54	0.17	0.84	0.24	0.73	1.16	0.40	0.88	0.33	0.32	0.27	0.21	0.39	0.13	0.23	1.15	0.14	0.73	2.97	2.20	2.28	0.74	1.88
$Z = Z_{\odot}$, Age = 13 Gyr																										
0	0.53	1.22	1.14	0.47	0.04	0.79	0.16	0.67	1.12	0.34	0.89	0.22	0.15	0.17	0.22	0.40	0.12	0.17	1.00	0.09	0.57	2.89	1.66	2.17	0.67	1.57
1	0.52	1.23	1.16	0.41	0.03	0.65	0.14	0.63	1.08	0.32	0.88	0.18	0.12	0.16	0.21	0.42	0.10	0.16	0.98	0.09	0.51	2.91	1.40	2.10	0.62	1.49
2	0.58	1.34	1.22	0.41	0.03	0.68	0.14	0.65	1.12	0.32	0.91	0.18	0.12	0.18	0.23	0.43	0.10	0.16	1.07	0.09	0.55	3.14	1.43	2.17	0.64	1.63
3	0.51	1.22	1.09	0.38	0.03	0.60	0.13	0.58	1.01	0.30	0.82	0.16	0.12	0.16	0.18	0.40	0.09	0.16	0.93	0.09	0.49	2.82	1.29	1.96	0.57	1.42
4	0.58	1.34	1.22	0.41	0.03	0.68	0.14	0.65	1.12	0.32	0.91	0.18	0.12	0.18	0.23	0.43	0.10	0.16	1.07	0.09	0.55	3.14	1.43	2.17	0.64	1.63
5	0.57	1.15	1.12	0.46	0.12	0.80	0.24	0.72	1.14	0.39	0.86	0.27	0.26	0.26	0.21	0.34	0.14	0.22	1.09	0.13	0.75	2.84	1.91	2.24	0.74	1.84

Note.
[a] IMF codes are as follows: 0—Salpeter (1955), 1—Chabrier (2003), 2—Kroupa (2001), 3—van Dokkum (2008), 4—Davé (2008), 5—dwarf-rich variant.

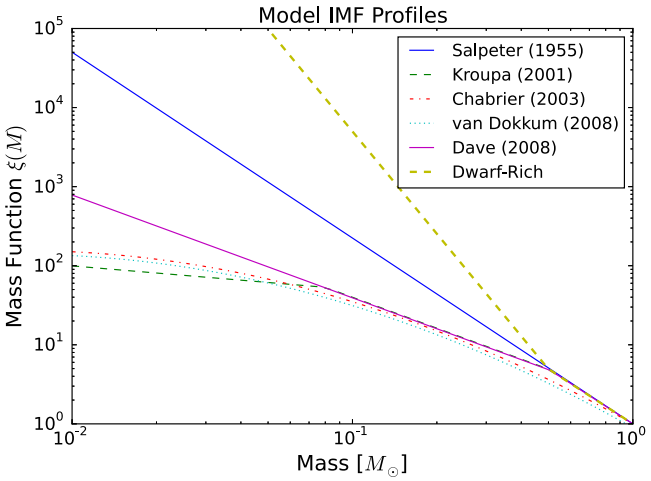

Figure 8. Mass profiles of each of the IMF models used in this work. All profiles are normalized at 1 $M_\odot$. Using each IMF as an input parameter in SSP modeling, we are able to measure the effects of a variable IMF on the EWs of our target metal lines. The results of this modeling are presented in Table 6.

lines), Salpeter (blue lines), and the dwarf-rich variant (red lines), which span our full range of low-mass IMF slopes. Overall, we see that the IMF is also an important factor, having a much stronger effect than metallicity and at least as comparable an effect as stellar age.

While there is some tension between our theoretical trends and those seen in other works (in particular, Cenarro et al. 2003 see an essentially flat EW trend with stellar age as opposed to our decreasing trend), this may not be entirely unexpected. Specifically, in evolutionary population synthesis there are significant uncertainties in the Hertzsprung–Russell diagram location of the core helium stage in very old populations and the double shell burning stage (asymptotic giant branch) in intermediate age populations. Although neither of these is the dominant light source at 1 μm, they are responsible for of the order of 10% of the light. We have simply used the default prescriptions in FSPS in the present paper but emphasize the caveat that line strength and age predictions in our current models are uncertain at levels of at least a few percent. These will need to be investigated further in our ongoing work with FSPS. Our model predictions regarding IMF dependence are on a firmer footing, as they are primarily influenced by the red giant branch and lower main-sequence ratio. By accounting for age and metallicity effects, however, we are able to better measure the intrinsic variations due to the IMF.

To demonstrate an IMF dependence that is less sensitive to metallicity effects, we plot the ratio of K I to Mg I as a function of σ. We choose K I for the numerator because it is a strong dwarf/giant discriminator and Mg I for the denominator because of its strong dependence on mass. Potassium is mostly ionized in the atmospheres of M dwarfs, but magnesium is not. As in the previous section, we sum the individual K I lines together to reduce noise, resulting in the ratio

$$R = \frac{\sum \mathrm{EW(K\ I)}}{\mathrm{EW(Mg\ I)}}. \quad (1)$$

The results, using our observed galaxy data, are shown in the upper left panel of Figure 10. The best-fit trend line to these data shows a significant correlation between line ratio and σ, given by $R = (0.6 \pm 0.2)\sigma_{100} + (1.16 \pm 0.25)$, where σ_{100} is σ expressed in units of 100 km s^{-1}. We do note that scatter in the data points could alter the slope, and the small sample size is subject to selection effects; however, the overall form of the trend is stable.

In the top right panel of Figure 10, we plot the expected K I / Mg I ratio for the theoretical models, assuming various IMF slopes. The black line assumes a stellar population with solar metallicity, while the red line uses a more metal-poor ($Z_{\rm gal} = Z_\odot/3$) model. The green line again assumes solar metallicity, but uses an older stellar population (13 Gyr) than either the black or red models (10 Gyr.) In all cases, we see that steeper IMF slopes predict a larger line ratio. While the magnitude of this effect is dependent on metallicity and stellar age, these changes are typically smaller than that of the IMF, diminishing their importance in the final result. While we do not explicitly test the effects of chemical abundance, we note that in the case of potassium Takeda et al. (2009) demonstrated that stars show only a mild trend in [K/Fe] abundance over the metallicity range populated by galaxies with $100 < \sigma < 350$ km s^{-1}. Because of this, potassium abundance should not play a significant role in the EW trends we see.

By comparing the two panels of the figure, we see that the measured data points have a similar shape to the model predictions, suggesting that the IMF is indeed variable, with low-mass galaxies favoring a Chabrier-like IMF and high-mass galaxies preferring a steeper, dwarf-heavy population, in agreement with other studies. Although the model prediction shows a shallower trend than the observed slope, the two plots are fully consistent with each other given the observational errors.

As a final comparison, we plot similar line ratios in the lower panels of Figure 10; however, here we substitute Ca II and Ti I, two elements that are already known to be sensitive to variations in the IMF. Like the K I ratio, these elements also show a slight trend favoring a bottom-heavy IMF in massive galaxies, though in both cases the correlation is less significant and there is more scatter in the data. Here again, the theory and observation trends agree with each other within the uncertainties. Other element lines have even noisier data, leading to less robust line fits. This is likely due to our small sample size, and future efforts with a larger galaxy sample will help to reduce statistical uncertainty. Regardless, these results, coupled with the more significant K I fit, are promising and do suggest some form of IMF variability.

6. Conclusions

We have presented the first results of a study looking for possible IMF-sensitive line features in the NIR ($\lambda = 1.1 - 1.3$ μm). For this pilot program we use a sample of eight massive, luminous ($L \sim 10L_*$), nearby galaxies, observing each with the *Magellan* FIRE spectrograph in order to maximize S/N and spectral coverage. We identify candidate lines using dwarf-star line catalogs (McLean et al. 2007; Deshpande et al. 2012) and also include the Ca II triplet (a known IMF-sensitive feature; van Dokkum & Conroy 2012) as a calibrator.

After identifying the lines, we measure EWs from the FIRE spectra and then look for correlations in the EW–mass plane. To trace total mass in each galaxy, we select two physical properties: K-band luminosity ($M_{\rm K}$) and central velocity dispersion (σ). While we do detect mild correlations between EW and luminosity, the best-fit trend lines are noisy and possibly driven by outliers. Conversely, the EW–σ relationships are nominally

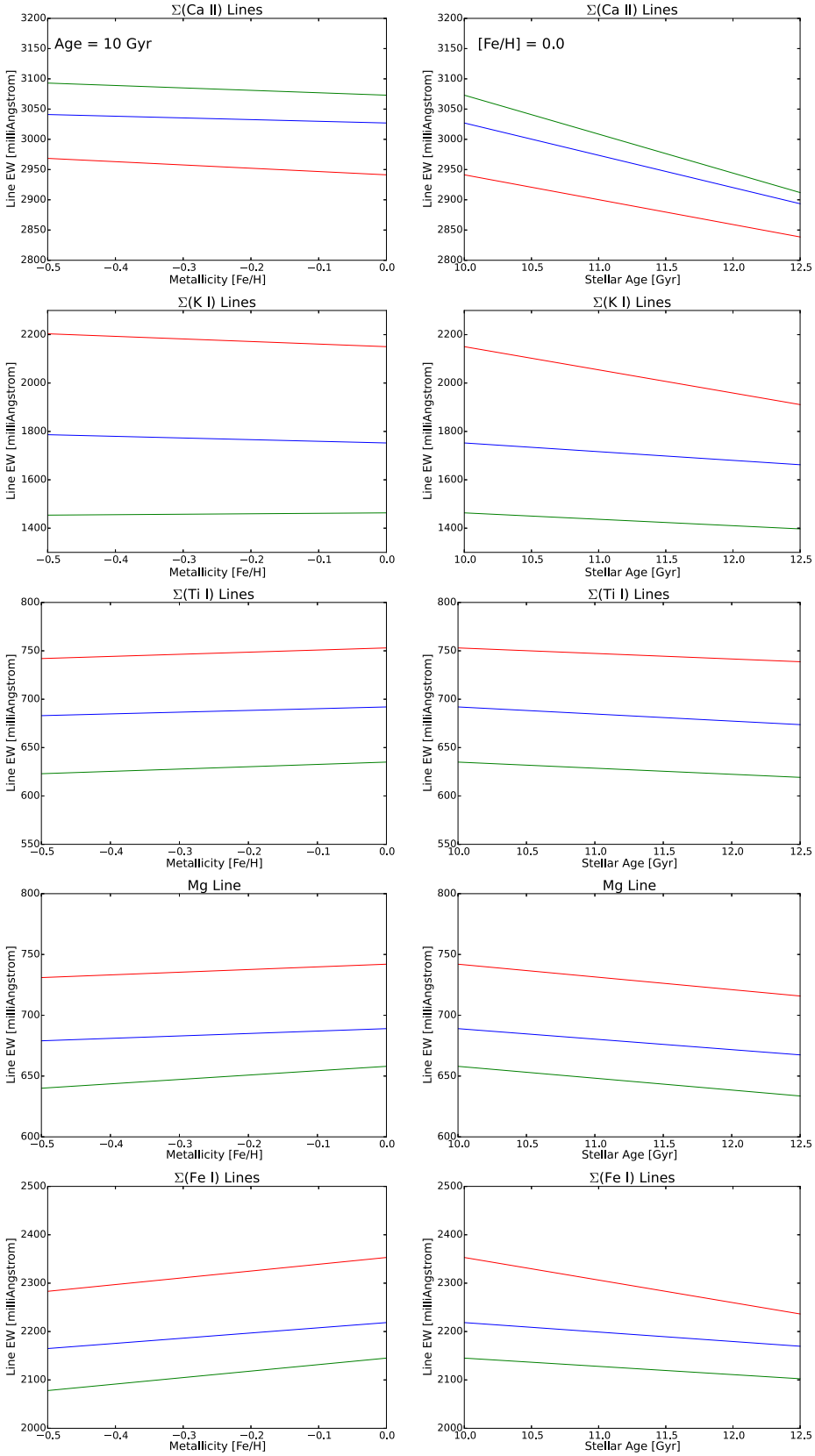

Figure 9. Variations in line EW as a function of metallicity and stellar age. Overall, we see that metallicity effects (left column) tend to be weaker than age effects (right column), but both play an important role. To avoid parameter degeneracies, the metallicity models are held at a fixed stellar age of 10 Gyr, while the age models are held at a fixed metallicity [Fe/H] = 0. To account for the IMF, we plot three different IMF codes: Salpeter (blue), Chabrier (green) and the dwarf-rich variant (red). We do see significant offsets between IMF models, which are larger than the variations due to metallicity and at least comparable to the variations due to stellar age. While the magnitude of the variations change with different IMF models, the general trend (positive or negative) of each element remains the same.

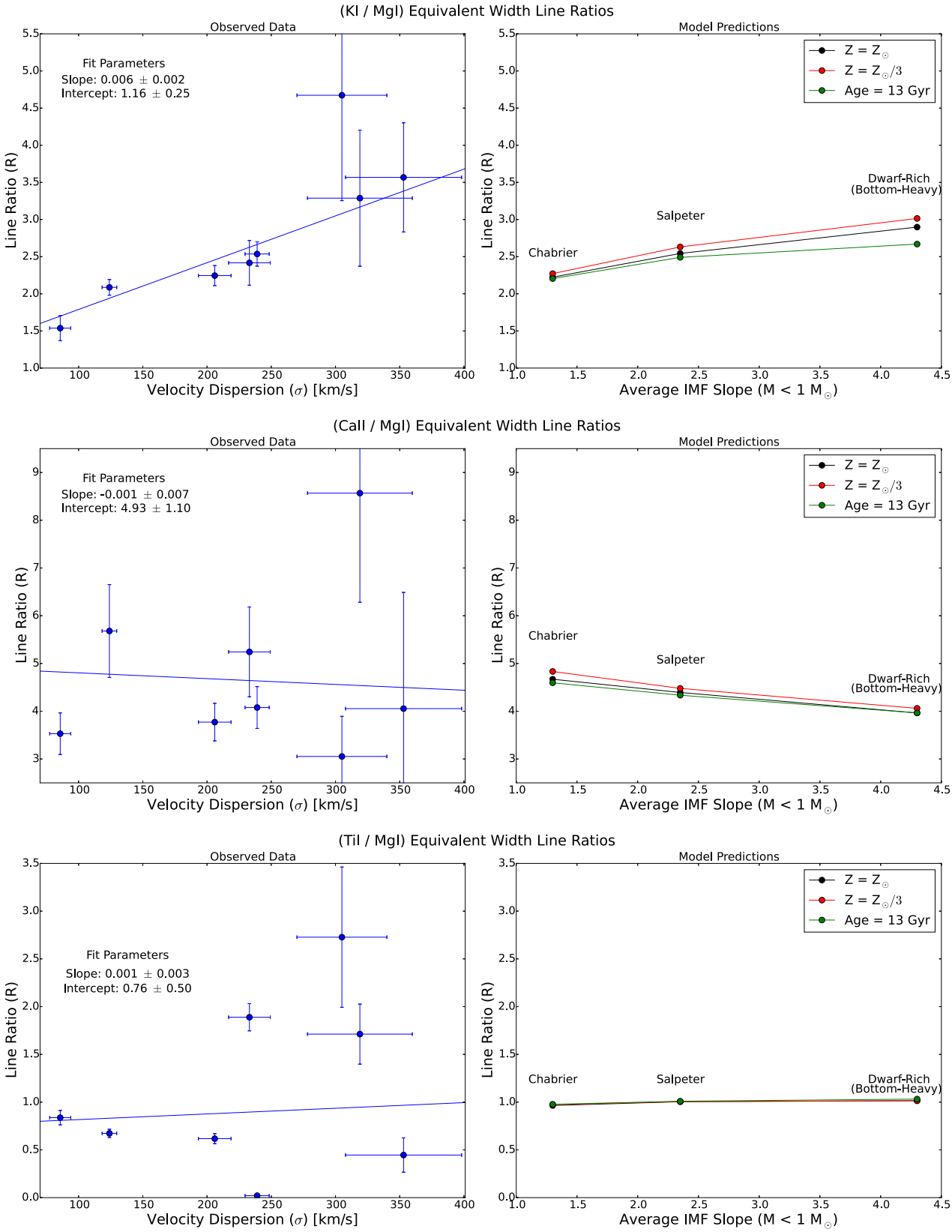

Figure 10. Top left: ratio of K I to Mg I line strengths as a function of velocity dispersion (σ). Ratios for each galaxy in the sample are shown as blue circles. A best-fit trend line can also be seen, highlighting a strong positive correlation between the two quantities. Top right: expected K I/ Mg I line ratios from the models based on the Conroy & Gunn (2010b) FSPS package, using three different IMF slopes. The black line represents models with $Z = Z_{\odot}$ metallicity, while the red line instead assumes a more metal-poor $Z = Z_{\odot}/3$ population. The green line again assumes a solar metallicity, but is for a stellar age of 13 Gyr instead of 10 Gyr. Lower panels: similar line ratios using Ca II and Ti I, elements that are already known to be IMF-sensitive. In both of these cases, we do see a moderate trend in the data and an agreement with the models; however, the slopes are not as significant and the scatter is larger.

tighter, with some elements showing a strong positive (possibly dwarf-sensitive) correlation (K I, Na I, Mn I), and others a negative (possibly giant-sensitive) correlation (Ca II, Mg I, Pa-β).

We probe the data for IMF dependence by taking the EW ratio (R) of K I to Mg I as a function of σ. After fitting a trend line to the data, we find a strong positive correlation given by $R = (0.6 \pm 0.2)\sigma_{100} + (1.16 \pm 0.25)$. Comparing this trend to the expected R value of theoretical models, this suggests a changing IMF: from dwarf-poor (Chabrier) in low-mass galaxies, to dwarf-rich in high-mass galaxies. While we do note the small sample size makes our data set susceptible to systematic bias and selection effects, our results are promising, even in the face of these limitations. Future efforts, involving a larger sample of galaxies, will likely improve our understanding of this phenomenon even further.

The authors wish to thank the referee for thoroughly reading the manuscript and providing several useful comments that greatly improved the quality of the paper. Thanks to Rob Simcoe for assistance with the FIRE pipeline. France Allard provided invaluable advice on synthetic stellar spectra. We also thank Blesson Mathew and Nidia Morrell for their contributions. We appreciate the use of Charlie Conroy's FSPS and Michele Cappellari's pPXF codes. D.J.L. acknowledges support from the ERC starting grant 336736-CALENDS. Parts of this research were conducted by the Australian Research Council Centre of Excellence for All-sky Astrophysics (CAASTRO), through project number CE110001020. D.A.F. thanks the ARC for financial support via DP130100388.

ORCID iDs

David J. Lagattuta https://orcid.org/0000-0002-7633-2883
Jeremy R. Mould https://orcid.org/0000-0003-3820-1740

References

Allard, F., Homeier, D., & Freytag, B. 2012, in IAU Symp. 282, From Interacting Binaries to Exoplanets: Essential Modeling Tools, ed. M. T. Richards & I. Hubeny (Cambridge: Cambridge Univ. Press), 235
Bruzual, G., & Charlot, S. 2003, MNRAS, 344, 1000
Cappellari, M., & Emsellem, E. 2004, PASP, 116, 138
Cappellari, M., McDermid, R. M., Alatalo, K., et al. 2013, MNRAS, 432, 1862
Cenarro, A. J., Gorgas, J., Vazdekis, A., Cardiel, N., & Peletier, R. F. 2003, MNRAS, 339, L12
Chabrier, G. 2003, PASP, 115, 763
Clauwens, B., Schaye, J., & Franx, M. 2015, MNRAS, 449, 4091
Conroy, C., & Gunn, J. E. 2010a, ApJ, 712, 833
Conroy, C., & Gunn, J. E. 2010b, FSPS: Flexible Stellar Population Synthesis, Astrophysics Source Code Library, ascl:1010.043
Conroy, C., Gunn, J. E., & White, M. 2009, ApJ, 699, 486
Conroy, C., & van Dokkum, P. 2012, ApJ, 747, 69
Conroy, C., & van Dokkum, P. G. 2012, ApJ, 760, 71
Conroy, C., van Dokkum, P. G., & Villaume, A. 2017, ApJ, 837, 166
Davé, R. 2008, MNRAS, 385, 147
Davé, R., Finlator, K., & Oppenheimer, B. D. 2012, MNRAS, 421, 98
Deshpande, R., Martín, E. L., Montgomery, M. M., et al. 2012, AJ, 144, 99
Dutton, A. A., Macciò, A. V., Mendel, J. T., & Simard, L. 2013, MNRAS, 432, 2496
Dutton, A. A., Mendel, J. T., & Simard, L. 2012, MNRAS, 422, 33
Ferreras, I., Weidner, C., Vazdekis, A., & La Barbera, F. 2015, MNRAS, 448, L82
Frogel, J. A., Becklin, E. E., Neugebauer, G., et al. 1975, ApJL, 195, L15
Graves, G. J., Faber, S. M., & Schiavon, R. P. 2009, ApJ, 693, 486
Kauffmann, G., & Charlot, S. 1998, MNRAS, 297, L23
Kroupa, P. 2001, MNRAS, 322, 231
La Barbera, F., Ferreras, I., Vazdekis, A., et al. 2013, MNRAS, 433, 3017
Leier, D., Ferreras, I., Saha, P., et al. 2016, MNRAS, 459, 3677
Lyubenova, M., Martín-Navarro, I., van de Ven, G., et al. 2016, MNRAS, 463, 3220
Makarov, D., Prugniel, P., Terekhova, N., Courtois, H., & Vauglin, I. 2014, A&A, 570, A13
Maraston, C. 2013, in IAU Symp. 295, The Intriguing Life of Massive Galaxies (Cambridge: Cambridge Univ. Pres), 272
Martín-Navarro, I., Pérez-González, P. G., Trujillo, I., et al. 2015a, ApJL, 798, L4
Martín-Navarro, I., Vazdekis, A., La Barbera, F., et al. 2015b, ApJL, 806, L31
McConnell, N. J., Lu, J. R., & Mann, A. W. 2016, ApJ, 821, 39
McLean, I. S., Prato, L., McGovern, M. R., et al. 2007, ApJ, 658, 1217
Meneses-Goytia, S., Peletier, R. F., Trager, S. C., & Vazdekis, A. 2015, A&A, 582, A97
Mould, J. 2014, arXiv:1403.1623
Posacki, S., Cappellari, M., Treu, T., Pellegrini, S., & Ciotti, L. 2015, MNRAS, 446, 493
Saglia, R. P., Maraston, C., Thomas, D., Bender, R., & Colless, M. 2002, ApJL, 579, L13
Salpeter, E. E. 1955, ApJ, 121, 161
Schiavon, R. P., Barbuy, B., Rossi, S. C. F., & Milone, A. 1997a, ApJ, 479, 902
Schiavon, R. P., Barbuy, B., & Singh, P. D. 1997b, ApJ, 484, 499
Simcoe, R. A., Burgasser, A. J., Bernstein, R. A., et al. 2008, Proc. SPIE, 7014, 70140U
Smith, R. J. 2014, MNRAS, 443, L69
Smith, R. J., Alton, P., Lucey, J. R., Conroy, C., & Carter, D. 2015, MNRAS, 454, L71
Spiniello, C., Trager, S., Koopmans, L. V. E., & Conroy, C. 2014, MNRAS, 438, 1483
Spiniello, C., Trager, S. C., & Koopmans, L. V. E. 2015, ApJ, 803, 87
Spiniello, C., Trager, S. C., Koopmans, L. V. E., & Chen, Y. P. 2012, ApJL, 753, L32
Takeda, Y., Kaneko, H., Matsumoto, N., et al. 2009, PASJ, 61, 563
Tremonti, C. A., Heckman, T. M., Kauffmann, G., et al. 2004, ApJ, 613, 898
Treu, T., Auger, M. W., Koopmans, L. V. E., et al. 2010, ApJ, 709, 1195
Vacca, W. D., Cushing, M. C., & Rayner, J. T. 2003, PASP, 115, 389
van der Marel, R. P., & Franx, M. 1993, ApJ, 407, 525
van Dokkum, P. G. 2008, ApJ, 674, 29
van Dokkum, P. G., & Conroy, C. 2012, ApJ, 760, 70